DOI: 10.13009/EUCASS2025-044
11TH EUROPEAN CONFERENCE FOR AERONAUTICS AND SPACE SCIENCES (EUCASS)

Actuator Layout Optimization Method for Mesh Reflector Shape Adjustment Based on Statistical Analysis

Siming, Liu, Shilin, Xie*† and Guowang, Luo**
** State Key Laboratory for Strength and Vibration of Mechanical Structures, Xi'an Jiaotong University*
Xi'an, PR China
slxie@mail.xjtu.edu.cn – lsm022117@stu.xjtu.edu.cn
† Corresponding Author

Abstract
Mesh reflectors, critical spacecraft subsystems requiring on-orbit shape adjustment, demand optimized actuator placement to balance performance and cost. Existing methods fail to provide universal actuator layout with comprehensive optimal performance under varying loads. To address above issues, this study proposes a statistical analysis-based optimization method. Potential actuator positions are defined; 3,000 stochastic load scenarios (assembly errors, thermal/stiffness loads) are simulated to derive optimal layouts per case, with statistical analysis finally determining the comprehensive optimal layout. Validated through simulations and experiments, this approach achieves high adjustment efficiency while providing universal actuator layout with comprehensive optimal performance under varying environmental disturbances.

1. Introduction

As a critical subsystem of spacecraft, mesh reflectors have become a focal point of research due to their ability to achieve large apertures, high stowage ratios, and low mass. To ensure optimal electromagnetic performance throughout their service life, on-orbit shape adjustment technology based on smart actuators is essential. A key aspect of this technology is the optimization of actuator layout, which is crucial for maintaining reflector performance while minimizing system complexity and cost.

Some researchers have studied the actuator layout optimization. Yuan et al. proposed the shape adjustment method to reduce shape distortion by automatically placing a small number of actuators at optimal locations.

However, these methods often fail to provide a unified actuator arrangement that is effective under varying load conditions. This limitation poses challenges for their application during on-orbit service, as the actuators in mesh reflectors cannot easily change positions once deployed.

To address the issue, a novel actuator placement optimization method for mesh reflector shape adjustment based on statistical analysis is proposed. Initially, we define potential actuator installation locations and set a limit on the total number of actuators. Considering the randomness and uncertainty of loads, 3,000 different random load scenarios, including cable assembly errors, thermal loads, and cable stiffness degradation loads, were simulated. For each scenario, the optimal distribution of actuator positions was analysed. Subsequently, the probability of each potential actuator installation location being selected as an optimal position across all scenarios was calculated. Based on the predefined number of actuators, the best installation locations were then determined.

The overall structure of the article is described as follows. In the section 2, the actuator placement optimization method is presented. In the section 3, the simulation study is conducted. The feasibility and effectiveness of the actuator placement optimization method are numerically demonstrated through a comparative study between the DMIA method and the finite element method. In the section 4, the DMIA method is experimentally validated based on a mesh reflector test model. In the section 5, the discussions and conclusions are presented.

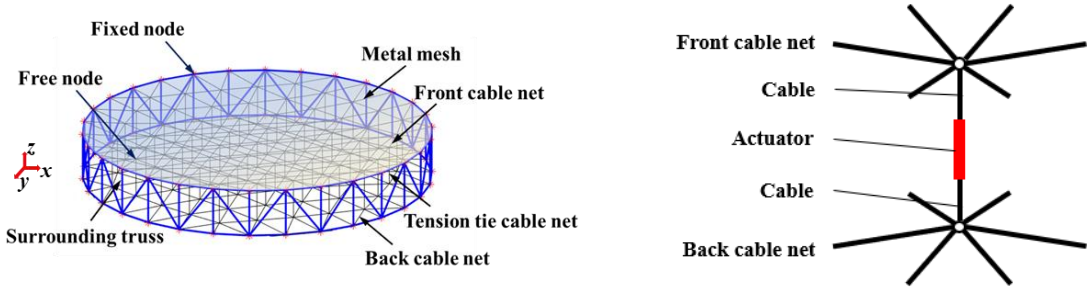
Copyright © 2025 by First Author. Posted online by the EUCASS association with permission.

DOI: 10.13009/EUCASS2025-044

2. Actuator layout optimization method

2.1 Mesh reflector configuration and actuating cable

As the shape adjustment object, the mesh reflector is first introduced. As illustrated in **Figure 1(a)**, this structure comprises two fundamental elements: a flexible cable net and a peripheral truss framework. The flexible cable net incorporates four essential constituents: the metal mesh, the front cable net, the tension tie cable net, and the back cable net. Structural nodes exhibit two distinct classifications - fixed nodes, which connected the truss and the cable nets, and free nodes, which connected the cables. A specialized actuation mechanism is implemented through an actuating cable where the actuator is embedded, as visually detailed in **Figure 1(b)**.



(a) Mesh reflector. (b) Actuating cable.

Figure 1: Mesh reflector and actuating cable.

2.2 Increment Expression of cable length and node coordinate

The length adjustment of cables via actuators enables the alteration of nodal coordinates in mesh reflectors, thereby modifying the reflector accuracy, which is defined as the root-mean-square (RMS) error of the node coordinates between the actual reflector and the ideal reflector. Consequently, establishing the mathematical relationship between cable length variations and corresponding nodal coordinate changes constitutes a fundamental requirement for effective shape adjustment.

There exists an equilibrium equation at each free node of the mesh reflector. By using a topology matrix that describes the connection relationships between nodes and cables, it can be simplified as follows,

$$\boldsymbol{C}^{\mathrm{T}}\boldsymbol{U}\boldsymbol{L}^{-1}\boldsymbol{t}=\boldsymbol{0} \tag{1}$$

Where $\boldsymbol{C}^{\mathrm{T}}$ is transposition of topological matrix, which could describe the relationship between nodes and cables. $\boldsymbol{U}$ is the diagonal matrix of node coordinate difference vectors, $\boldsymbol{L}^{-1}$ is the diagonal matrix of reciprocal vector of cable length, $\boldsymbol{t}$ is the cable tension vector.

In the shape adjustment, the equilibrium equation is a function of the cable length without pre-tension and the free node coordinates,

$$f(\boldsymbol{X}_{free},\boldsymbol{l}_0)=\boldsymbol{C}^{\mathrm{T}}\boldsymbol{U}\boldsymbol{L}^{-1}\boldsymbol{t} \tag{2}$$

Where $\boldsymbol{X}_{free}$ is the free node coordinate vector, $\boldsymbol{l}_0$ is the cable length vector without pre-tension.

After the actuator is locked, the equation will reach a new equilibrium,

$$f(\boldsymbol{X}_{free}+\Delta\boldsymbol{X}_{free},\boldsymbol{l}_0+\Delta\boldsymbol{l}_0)=\boldsymbol{0} \tag{3}$$

Expand the above equation at ($\boldsymbol{X}_{free}$, $\boldsymbol{l}_0$), and retain the first-order term of Taylor series,

$$f(\boldsymbol{X}_{free}+\Delta\boldsymbol{X}_{free},\boldsymbol{l}_0+\Delta\boldsymbol{l}_0)=f(\boldsymbol{X}_{free},\boldsymbol{l}_0)+\frac{\partial f(\boldsymbol{X}_{free},\boldsymbol{l}_0)}{\partial \boldsymbol{X}_{free}}\mathrm{d}\boldsymbol{X}_{free}+\frac{\partial f(\boldsymbol{X}_{free},\boldsymbol{l}_0)}{\partial \boldsymbol{l}_0}\mathrm{d}\boldsymbol{l}_0 \tag{4}$$

The coefficient matrix before the increment of free node coordinates can be expressed as,

$$\frac{\partial f(\boldsymbol{X}_{free},\boldsymbol{l}_0)}{\partial \boldsymbol{X}_{free}}=\boldsymbol{C}^{\mathrm{T}}\left(\boldsymbol{L}^{-1}\boldsymbol{T}+\boldsymbol{U}\boldsymbol{T}\frac{\partial \boldsymbol{l}^{-1}}{\partial \boldsymbol{u}}+\boldsymbol{U}\boldsymbol{L}^{-1}\frac{\partial \boldsymbol{t}}{\partial \boldsymbol{u}}\right) \tag{5}$$

The coefficient matrix before the cable length matrix without pre-tension can be expressed as,

$$\frac{\partial f(\boldsymbol{X}_{free},\boldsymbol{l}_0)}{\partial \boldsymbol{l}_0}=\boldsymbol{C}^{\mathrm{T}}\boldsymbol{U}\boldsymbol{L}^{-1}\frac{\partial \boldsymbol{t}}{\partial \boldsymbol{l}_0} \tag{6}$$

Therefore,

$$\Delta\boldsymbol{X}_{free}=\boldsymbol{K}\Delta\boldsymbol{l}_0 \tag{7}$$

DOI: 10.13009/EUCASS2025-044

According to whether the cable is embedded in the actuator, it can be divided into actuating cables and ordinary cables. Eq.(7) is divided into blocks based on the type of cable as follows,

$$\Delta \boldsymbol{X}_{free} = \begin{bmatrix} \Delta \boldsymbol{X}_f \\ \Delta \boldsymbol{X}_b \end{bmatrix} = \begin{bmatrix} \boldsymbol{K}_{fa} & \boldsymbol{K}_{fs} \\ \boldsymbol{K}_{ba} & \boldsymbol{K}_{bs} \end{bmatrix} \begin{bmatrix} \Delta \boldsymbol{l}_0^a \\ \Delta \boldsymbol{l}_0^s \end{bmatrix} \tag{8}$$

Where $\Delta \boldsymbol{X}_f$ is the coordinate vector of free nodes in the front cable net, $\Delta \boldsymbol{X}_b$ is the coordinate vector of free nodes in the back cable net, $\Delta \boldsymbol{l}_0^a$, $\Delta \boldsymbol{l}_0^s$ are the length change vectors of the actuating cables and ordinary cables, respectively.

The ordinary cable length without pretension will not change. The node coordinate vector in the front cable net can be represented as,

$$\Delta \boldsymbol{X}_f = \boldsymbol{K}_{fa} \Delta \boldsymbol{l}_0^a \tag{9}$$

2.3 Actuator layout optimization model for shape adjustment

Once the relationship between node coordinates and actuating cable lengths is established, the shape adjustment model could be established. At this point, we can transform the shape adjustment model into the actuator layout optimization model by adding a filtering coefficient,

$$\Delta \boldsymbol{X}_f = \boldsymbol{K}_{fa} \cdot \boldsymbol{\Gamma} \cdot \Delta \boldsymbol{l}_0^a \tag{10}$$

Where $\boldsymbol{\Gamma}$=diag$\left(\left[\Gamma_1, \Gamma_2, \mathrm{L}\ , \Gamma_m\right]^{\mathrm{T}}\right)$, $\Gamma_i = 0$ or 1.

The actuator layout optimization model for shape adjustment can be formulated based on the reflector accuracy deviation of the reflector. Within this framework, the first step involves quantifying the surface accuracy in terms of cable length variations through Eq.(10). The reflector accuracy is defined as the root mean square error of the node coordinates between the actual reflector and the ideal reflector,

$$\delta_{rms} = \sqrt{\frac{1}{N_f} \sum_{i=1}^{N_f} \delta_i^2} \tag{11}$$

Where δ_{rms} is the reflector accuracy, δ_i is the displacement deviation of the i-th node in the antenna focal axis direction between the actual reflector and the ideal reflector in the front cable net, N_f is the number of free nodes in the front cable net.

The ideal reflector a parabolic surface, which could be expressed as,

$$z = \frac{1}{4 f_c}\left(x^2 + y^2\right) + h \tag{12}$$

Therefore, δ_i could be expressed as follows,

$$\delta_i = z_{i_{ideal}} - z_{i_{actual}} = \frac{1}{4 f_c}\left(x_{fi}^2 + y_{fi}^2\right) + h - z_{fi} \tag{13}$$

When performing shape adjustment, the cable lengths change, result in the change in node coordinates,

$$\delta_i = \frac{1}{4 f_c}\left(\left(x_{fi} + \Delta x_{fi}\right)^2 + \left(y_{fi} + \Delta y_{fi}\right)^2\right) + h - \left(z_{fi} + \Delta z_{fi}\right) \tag{14}$$

Where, $\Delta \boldsymbol{x}_{fi}$, $\Delta \boldsymbol{y}_{fi}$, $\Delta \boldsymbol{z}_{fi}$ is the increment of node coordinates in x, y, z directions, respectively.

The high-order small quantities in Eq.(14) could be ignored,

$$\delta_i = \frac{1}{2 f_c}\left(x_{fi} \Delta x_{fi} + y_{fi} \Delta y_{fi}\right) - \Delta z_{fi} + \frac{1}{4 f_c}\left(x_{fi}^2 + y_{fi}^2\right) + h - z_{fi} \tag{15}$$

Write it in matrix form,

$$\delta_i = \boldsymbol{p}_i \Delta \boldsymbol{X}_{fi} + q_i \tag{16}$$

Where, $\boldsymbol{p}_i = \left[x_{fi} \middle/ 2 f_c, y_{fi} \middle/ 2 f_c, -1 \right]$, $\Delta \boldsymbol{X}_{fi} = \left[\Delta x_{fi}, \Delta y_{fi}, \Delta z_{fi}\right]^{\mathrm{T}}$, $q_i = 1 \middle/ 4 f \left(x_{fi}^2 + y_{fi}^2\right) + h - z_{fi}$.

According to Eq.(11), the reflector accuracy could be expressed as,

$$\sum_{i=1}^{N_f} \delta_i^2 = \left(\Delta \boldsymbol{x}_a\right)^{\mathrm{T}} \boldsymbol{P}_K^{\mathrm{T}} \boldsymbol{P}_K \Delta \boldsymbol{x}_a + \boldsymbol{Q}^{\mathrm{T}} \boldsymbol{Q} \tag{17}$$

Where, $\boldsymbol{P}_K = \boldsymbol{P} \boldsymbol{K}_{fa} \boldsymbol{K}_{c-a}$, $\boldsymbol{K}_{c-a} = \mathrm{diag}\left(\left[k_{c-a}^1, k_{c-a}^2, \mathrm{L}\ , k_{c-a}^{n_a}\right]^{\mathrm{T}}\right)$, n_a is the number of actuators.

DOI: 10.13009/EUCASS2025-044

Based on Eq.(17), the shape adjustment optimization model can be established. The optimization variables are the actuation displacements of each actuator. The objective function is to minimize the reflector accuracy. The constraints include that the actuator displacements must not exceed their maximum stroke, and the actuators must not exceed their maximum force range.

$$\begin{aligned} &\text{find } \Delta\boldsymbol{x}_a = \left[\Delta x_a^1, \Delta x_a^2, \mathrm{L}\ , \Delta x_a^{n_a}\right]^{\mathrm{T}} \quad \& \ \boldsymbol{\Gamma} = \mathrm{diag}\left(\left[\Gamma_1, \Gamma_2, \mathrm{L}\ , \Gamma_m\right]^{\mathrm{T}}\right) \\ &\min\ f = \sum_{i=1}^{N_f} \delta_i^2 = \left(\Delta\boldsymbol{x}_a\right)^{\mathrm{T}} \boldsymbol{P}_K^{\mathrm{T}} \boldsymbol{P}_K \Delta\boldsymbol{x}_a + \boldsymbol{Q}^{\mathrm{T}}\boldsymbol{Q} \\ &\text{s.t.} \begin{cases} \Delta x_a^i \le \Delta x_{ub} \\ \Delta x_a^i \ge \Delta x_{lb} \end{cases} \ \& \ \begin{cases} t_a + \Delta t_a \ge 0 \\ t_a + \Delta t_a \le t_a^{\max} \end{cases} \ \& \ \sum_{j=1}^{n_a} \Gamma_j = N_{act} \end{aligned} \tag{18}$$

Where Δx_{ub} is the maximum stroke of the actuators, Δx_{lb} is the minimum stroke of the actuators, $t_a^{\max}$ is the maximum static friction of the actuator locking mechanism.

The current actuator optimization method can effectively optimize actuator layouts under different environmental disturbances. However, the optimized results are environment-dependent—that is, different environmental loads correspond to different optimal layouts. In practice, once actuators are embedded into the mesh reflector, their positions can hardly be adjusted, making such environment-specific optimization schemes infeasible. To address the problem, the actuator layout optimization method based on the statistical analysis is proposed.

Randomly simulate N_{scene} different scenarios, with the number of actuators limited to N_{act}. For the k=1 scenario, there will be an optimal actuator layout $\left\{ p_k^{(i)} \right\}_{k=1}^{M}$, where $p_k^{(i)} \in \{0,1\}$ indicates whether the i-th potential actuator installation position on the mesh reflector is selected for actuator installation in the k-th scenario. If selected, $p_k^{(i)} = 1$; otherwise, $p_k^{(i)} = 0$. M represents the total number of potential actuator installation positions.

After computing the N_{scene} different scenarios, the probability of the i-th position being selected as an actuator embedded position can be calculated.

$$\rho_i = \frac{1}{N_{scene}} \sum_{k=1}^{N_{scene}} p_k^{(i)} \quad (i = 1,2,\mathrm{L}\ ,M) \tag{19}$$

Where, ρ_i represents the probability that the i-th position is selected as the actuator embedding position in all scenarios. The actuator layout optimization model could be described as follows,

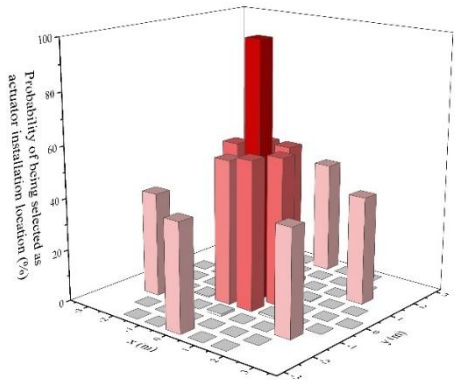
$$\begin{aligned} &\text{find } \boldsymbol{\lambda} = [\lambda_1, \lambda_2, \mathrm{L}\ , \lambda_M]^{\mathrm{T}} \\ &\max \sum_{i=1}^{M} \rho_i \lambda_i \\ &\text{s.t.} \sum_{i=1}^{M} \lambda_i = N_{act} \end{aligned} \tag{20}$$

Where $\boldsymbol{\lambda}$ is the re-filtering vector.

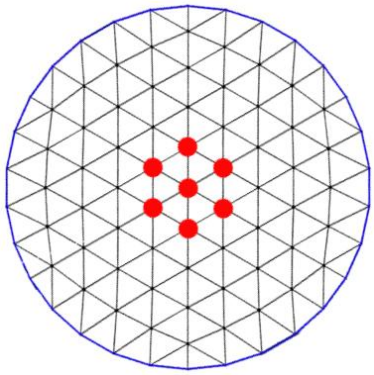
3. Simulation Studies

The complex loads that mesh reflectors are mainly subjected to include cable assembly errors, thermal loads, and cable degradation loads. Therefore, a total of 3000 scenarios were randomly simulated, including 1000 scenarios considering only assembly error loads, 1000 scenarios considering only thermal load effects, and 1000 scenarios considering only cable stiffness degradation loads. The probabilities of different positions being selected for embedding actuators were obtained, as shown in **Figure 2**. Finally, the optimized actuator layout for different numbers of actuators were derived as follows,

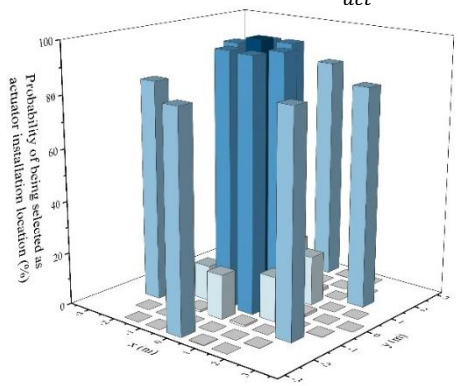
DOI: 10.13009/EUCASS2025-044



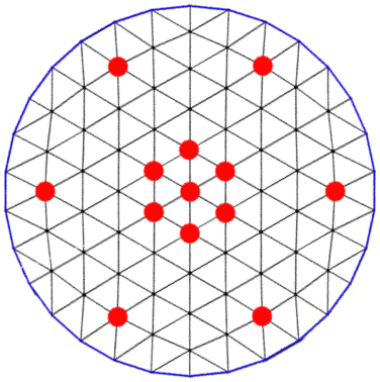
(a) Probability of being selected as actuator installation location when $N_{act} = 7$



(b) Optimized actuator layout when $N_{act} = 7$



(c) Probability of being selected as actuator installation location when $N_{act} = 13$



(d) Optimized actuator layout when $N_{act} = 13$

Figure 2. Optimized actuator layout for different numbers of actuators.

The optimized actuator layouts were adopted to adjust the mesh reflector under the assemble error, thermal load and cable stiffness degradation, and the reflector accuracy and shape adjustment effect are shown in **Table 1**,

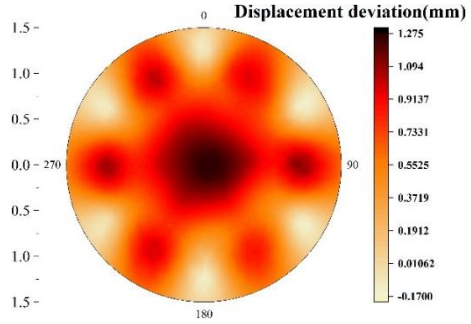
Table 1. Reflector accuracy and shape adjustment effect for different numbers of actuators.

Condition	Reflector accuracy (mm) with $N_{act} = 7$	η with $N_{act} = 7$	Reflector accuracy (mm) with $N_{act} = 13$	η with $N_{act} = 13$
Initial reflector deteriorated by assemble error	0.792			
After 1st adjustment	0.657	17.06%	0.608	23.26
Reflector deteriorated by thermal load	0.494		0.495	
After 2nd adjustment	0.275	44.33%	0.221	55.35%
Reflector deteriorated by cable stiffness degradation	0.614		0.575	
After 3th adjustment	0.512	16.61%	0.442	23.13%

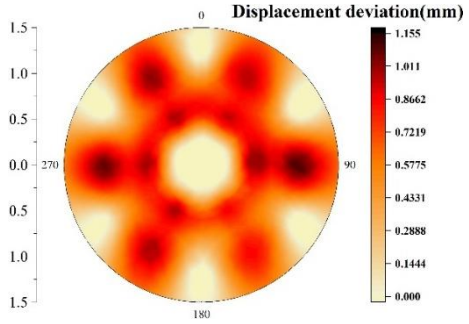
It is worth mentioning that the reflector accuracy only reflects the overall displacement difference of mesh reflector, but cannot show local difference. To better represent the displacement changes of each node in the reflector before and after adjustment, displacement deviation cloud charts were introduced. Note that the displacement deviation cloud chart can display the displacement deviation between each node in the real reflector and the corresponding node in the ideal reflector. Although the reflector is a three-dimensional surface, it can be projected onto the *x*-*y* plane and uniquely

DOI: 10.13009/EUCASS2025-044

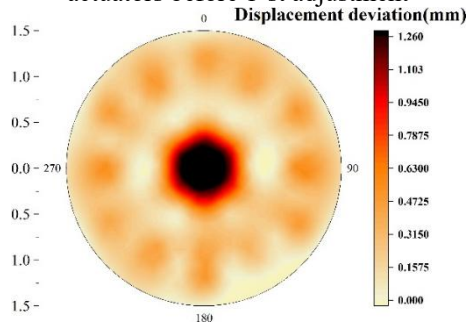
represented by the *x* and *y* coordinates of the nodes in the front cable net. Therefore, in the displacement deviation cloud chart, the *x*-*y* plane can be used to observe the displacement deviation of each node in the reflector. The local variation of the reflector can be more intuitively observed from the displacement deviation cloud chart. Therefore, to present the results in Section 4.4 more sufficient, the displacement deviation cloud charts of the reflectors using 7 actuators and 13 actuators are shown in **Figure 3** and **4**.



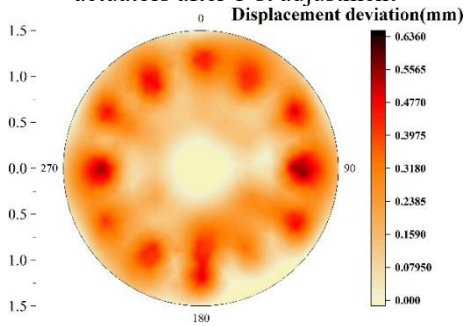
(a) Displacement deviation cloud chart using 7 actuators before 1-st adjustment



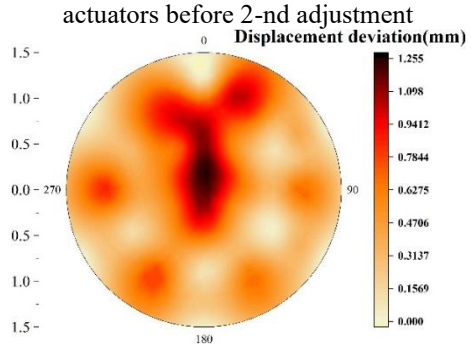
(b) Displacement deviation cloud chart using 7 actuators after 1-st adjustment



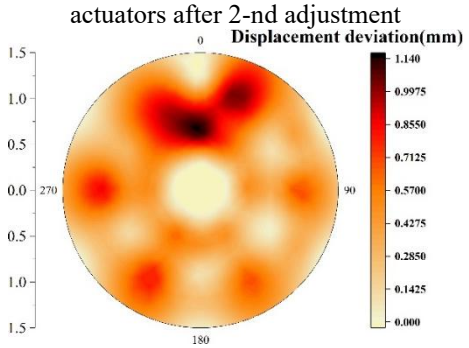
(c) Displacement deviation cloud chart using 7 actuators before 2-nd adjustment



(d) Displacement deviation cloud chart using 7 actuators after 2-nd adjustment

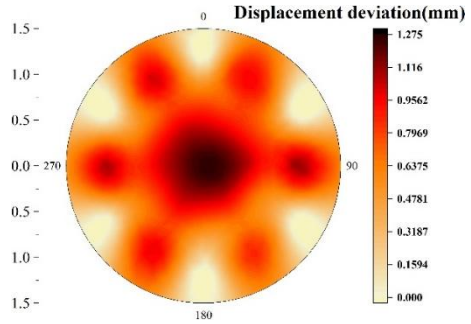


(e) Displacement deviation cloud chart using 7 actuators before 3-th adjustment

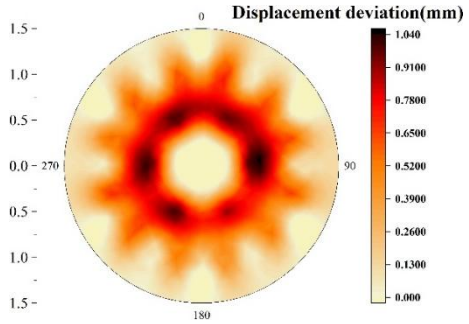


(f) Displacement deviation cloud chart using 7 actuators after 3-th adjustment

Figure 3. Displacement deviation cloud charts of the reflectors using 7 actuators.

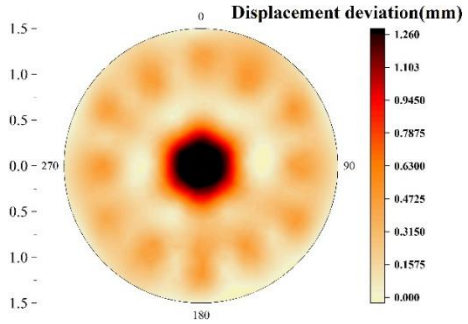


(a) Displacement deviation cloud chart using 13 actuators before 1-st adjustment

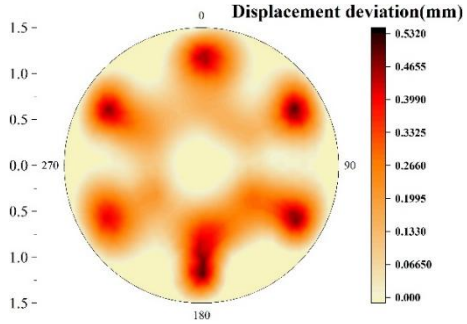


(b) Displacement deviation cloud chart using 13 actuators after 1-st adjustment

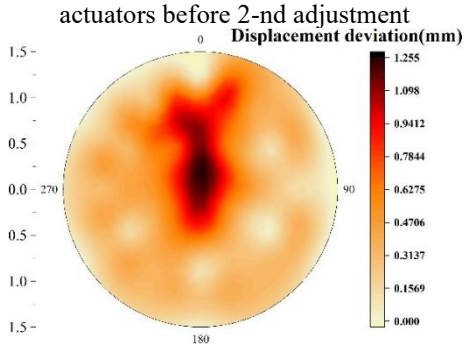
DOI: 10.13009/EUCASS2025-044



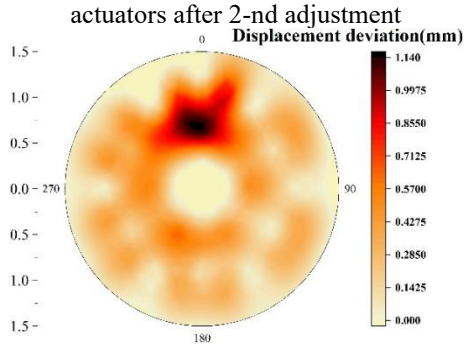
(c) Displacement deviation cloud chart using 13 actuators before 2-nd adjustment



(d) Displacement deviation cloud chart using 13 actuators after 2-nd adjustment



(e) Displacement deviation cloud chart using 13 actuators before 3-th adjustment



(f) Displacement deviation cloud chart using 13 actuators after 3-th adjustment

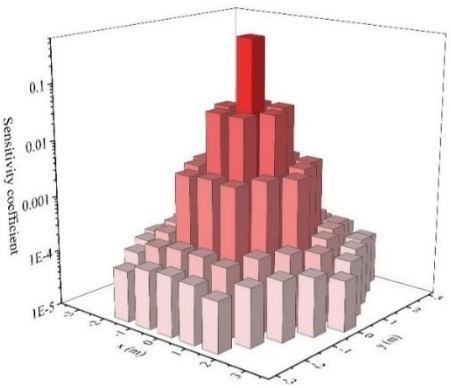
Figure 4. Displacement deviation cloud charts of the reflectors using 13 actuators.

From **Table 1**, **Figure 3** and **4**, it can be observed that as the number of actuators decreases, the control effectiveness of the actuators declines significantly. To explain this phenomenon, the sensitivity coefficient is introduced. The physical meaning of the sensitivity coefficient is the magnitude of the displacement change at the *i*-th node corresponding to a unit change in the length of the *j*-th actuating cable.

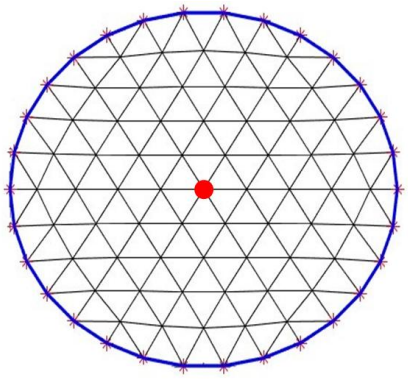
$$S_{ij} = \frac{\partial d_i}{\partial l_j} \tag{21}$$

Where, S_{ij} is the sensitivity coefficient, d_i is the displacement of the *i*-th node.

The sensitivity coefficient of the tension tie cable is shown in **Figure 5**,



(a) Sensitivity coefficient S_{ij} bar chart of mesh reflector with *i*=1



(b) *i*=1 corresponds to the location of the actuator in the top view of the mesh reflector

Figure 5. Sensitivity coefficient with *i*=1.

From **Figure 5**, when the tension changes of actuating cables cause node displacement variations in the front net, the primary impact is on the nodes connected to the actuating cables and their nearby nodes. As the distance increases, the influence of the actuating cables decreases exponentially. Therefore, the optimized actuator layout may not be

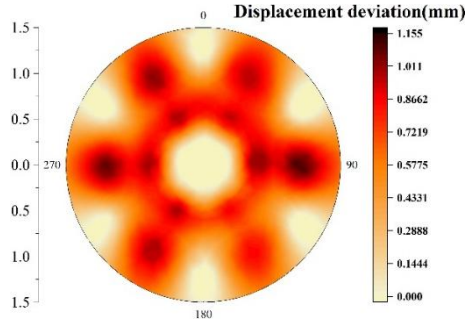
DOI: 10.13009/EUCASS2025-044

able to precisely correct local reflector accuracy deterioration, but it can provide a certain degree of control over global reflector accuracy deterioration.

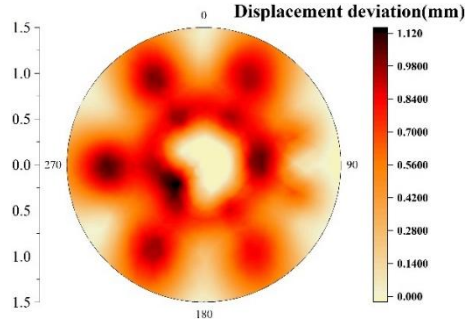
To compare the effectiveness of the actuator layout optimization method based on statistical analysis and the actuator layout optimization method proposed by Yuan, we used Yuan's method to calculate the same simulation case. The comparison results are shown in **Table 2**, **Figure 4**. Since the potential embedded positions of actuators correspond to tension tie cables that maintain a one-to-one relationship with the nodes in the front cable net, the optimized actuator layout is visualized through a two-dimensional top view of the mesh reflector. And the comparison of actuator layout optimization results is shown in **Figure 5**.

Table 2. Comparison of the reflector accuracy between the actuator layout optimization method based on statistical analysis and the actuator layout optimization method proposed by Yuan

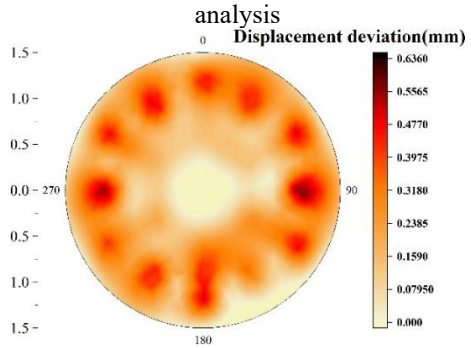
Actuator number	Method	Initial reflector deteriorated by assemble error	After 1st adjustment	Reflector deteriorated by thermal load	After 2nd adjustment	Reflector deteriorated by cable stiffness degradation	After 3th adjustment
$N_{act} = 7$	statistical analysis	0.792 mm	0.657 mm	0.494 mm	0.275 mm	0.614 mm	0.512 mm
	Yuan	0.792 mm	0.655 mm	0.494 mm	0.275 mm	0.614 mm	0.490mm
$N_{act} = 13$	statistical analysis	0.792 mm	0.608 mm	0.495 mm	0.221 mm	0.575 mm	0.442 mm
	Yuan	0.792 mm	0.601 mm	0.495 mm	0.221 mm	0.575 mm	0.406mm



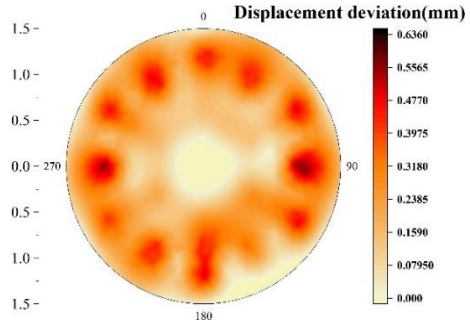
(a) Displacement deviation cloud chart using 7 actuators after 1-st adjustment by the actuator layout optimization method based on statistical analysis



(b) Displacement deviation cloud chart using 7 actuators after 1-st adjustment by the actuator layout optimization method proposed by Yuan

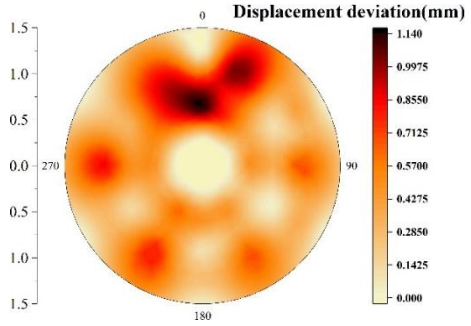


(c) Displacement deviation cloud chart using 7 actuators after 2-nd adjustment by the actuator layout optimization method based on statistical analysis

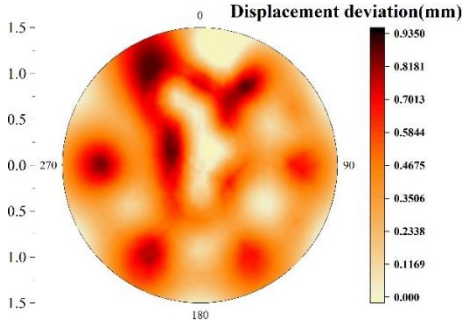


(d) Displacement deviation cloud chart using 7 actuators after 2-nd adjustment by the actuator layout optimization method proposed by Yuan

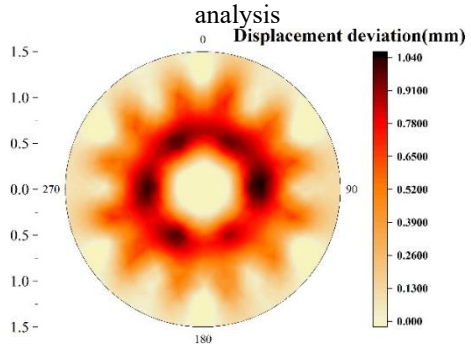
DOI: 10.13009/EUCASS2025-044



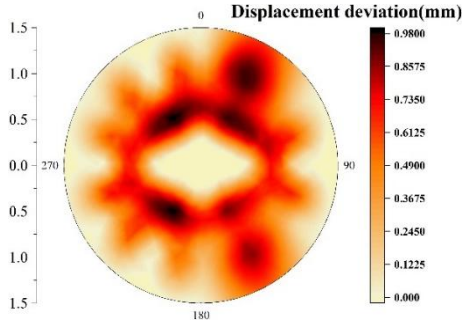
(e) Displacement deviation cloud chart using 7 actuators after 3-th adjustment by the actuator layout optimization method based on statistical analysis



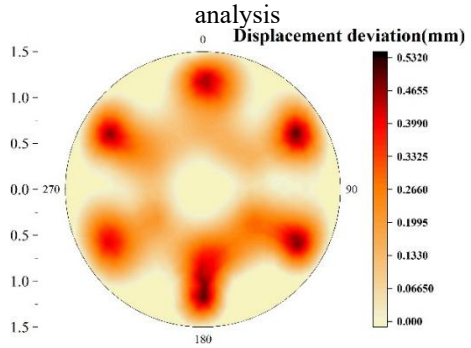
(f) Displacement deviation cloud chart using 7 actuators after 3-th adjustment by the actuator layout optimization method proposed by Yuan



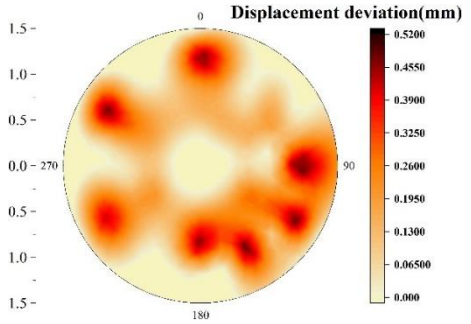
(g) Displacement deviation cloud chart using 13 actuators after 1-st adjustment by the actuator layout optimization method based on statistical analysis



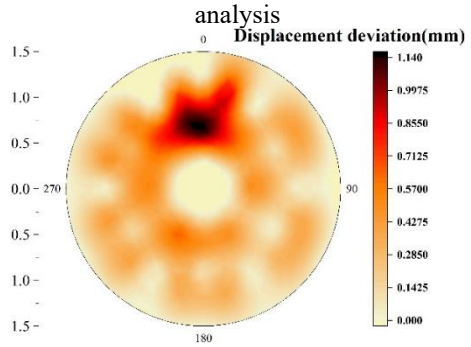
(h) Displacement deviation cloud chart using 13 actuators after 1-st adjustment by the actuator layout optimization method proposed by Yuan



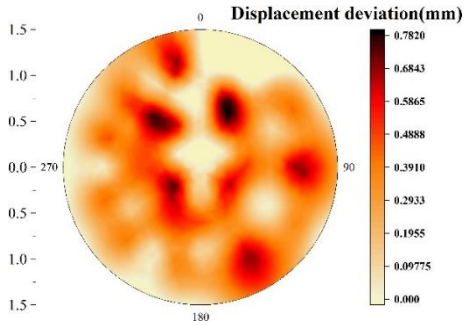
(i) Displacement deviation cloud chart using 13 actuators after 2-nd adjustment by the actuator layout optimization method based on statistical analysis



(j) Displacement deviation cloud chart using 13 actuators after 2-nd adjustment by the actuator layout optimization method proposed by Yuan



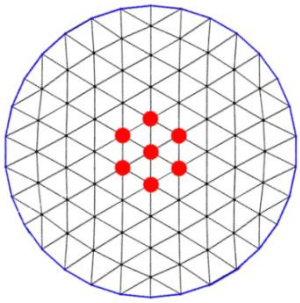
(k) Displacement deviation cloud chart using 13 actuators after 3-th adjustment by the actuator layout optimization method based on statistical analysis



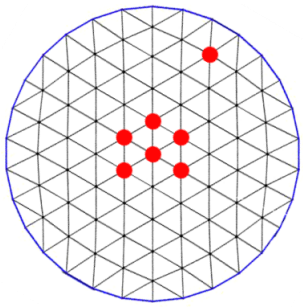
(l) Displacement deviation cloud chart using 13 actuators after 3-th adjustment by the actuator layout optimization method proposed by Yuan

Figure 4. Comparison of displacement deviation of cloud charts of the reflectors between the actuator layout optimization method based on statistical analysis and the actuator layout optimization method proposed by Yuan.

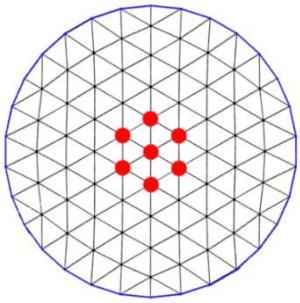
DOI: 10.13009/EUCASS2025-044



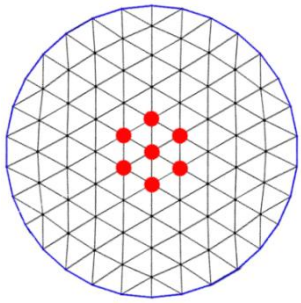
(a) Actuator layout obtained by the actuator layout optimization method based on statistical analysis in the 1-st adjustment using 7 actuators



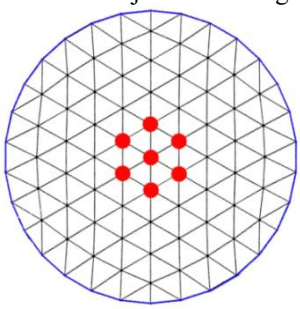
(b) Actuator layout obtained by the actuator layout optimization method proposed by Yuan in the 1-st adjustment using 7 actuators



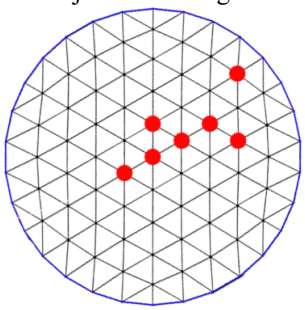
(c) Actuator layout obtained by the actuator layout optimization method based on statistical analysis in the 2-nd adjustment using 7 actuators



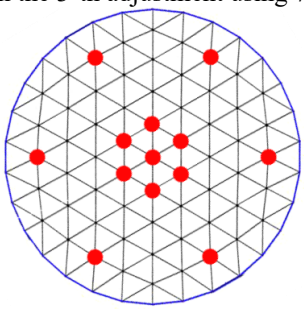
(d) Actuator layout obtained by the actuator layout optimization method proposed by Yuan in the 2-nd adjustment using 7 actuators



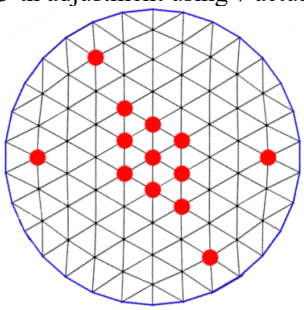
(e) Actuator layout obtained by the actuator layout optimization method based on statistical analysis in the 3-th adjustment using 7 actuators



(f) Actuator layout obtained by the actuator layout optimization method proposed by Yuan in the 3-th adjustment using 7 actuators

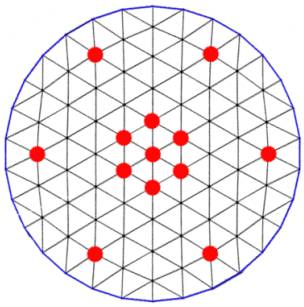


(g) Actuator layout obtained by the actuator layout optimization method based on statistical analysis in the 1-st adjustment using 13 actuators

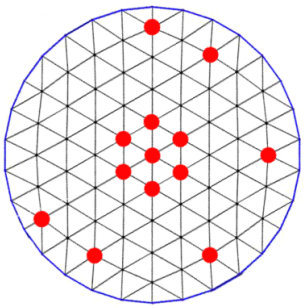


(h) Actuator layout obtained by the actuator layout optimization method proposed by Yuan in the 1-st adjustment using 13 actuators

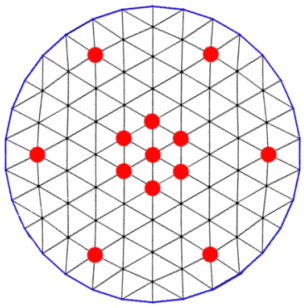
DOI: 10.13009/EUCASS2025-044



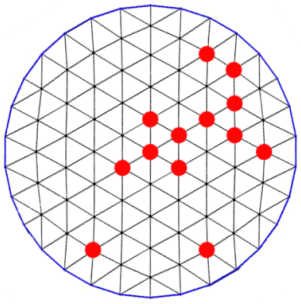
(i) Actuator layout obtained by the actuator layout optimization method based on statistical analysis in the 2-nd adjustment using 13 actuators



(j) Actuator layout obtained by the actuator layout optimization method proposed by Yuan in the 2-nd adjustment using 13 actuators



(k) Actuator layout obtained by the actuator layout optimization method based on statistical analysis in the 3-th adjustment using 13 actuators



(l) Actuator layout obtained by the actuator layout optimization method proposed by Yuan in the 3-th adjustment using 13 actuators

Figure 5. Comparison of the sensor layout results obtained between the actuator layout optimization method based on statistical analysis and the actuator layout optimization method proposed by Yuan.

Firstly, regarding the optimization outcomes of reflector accuracy in **Table 6**, under identical actuator quantities, the Yuan-optimized actuator layout demonstrates marginally superior reflector accuracy compared to the statistical analysis method, with a maximum discrepancy of 0.036 mm. As evidenced by **Figure 5**, however, enhanced reflector accuracy is achieved through modifications to the actuator layout—a parameter adjustment that proves impractical during the operational phase of mesh reflectors. In contrast, the statistical analysis method enables effective accuracy regulation without requiring layout alterations, thereby establishing itself as a more practical and robust optimization methodology for actuator layout.

4. Experimental Studies

4.1 Experiment setup

To verify the actuator layout optimization method of mesh reflectors, a mesh reflector test model with a height of 0.5m and a diameter of 1.5m was fabricated. The mesh reflector test model has the same configuration as the simulation model, consisting of a surrounding truss, front cable net, tension tie cable net, and back cable net. The 0.4mm nylon cables were used to form the mesh reflector cable net structure. Nylon cables are more homogeneous compared to woven cables. By measuring the stiffness of multiple nylon cables of the same length, it was found that the stiffness change did not exceed 3% of the calibration value.

The surrounding truss is composed of circular steel pipes with the outer diameter of 30mm and the thickness of 3mm. Since the deployment process is not considered in this experiment, the steel pipes are welded together. Meanwhile, finite element simulation was conducted to verify that the deformation of the truss under cable tensions does not affect the reflector. In finite element simulation, the maximum deformation of the truss shall not exceed 2×10^{-3}mm. Therefore, the truss could be treated as a rigid structure.

The experimental validation of actuator layout optimization method for mesh reflector is shown in **Figure 5**. In the experiment, the influence of gravity cannot be ignored. Therefore, the method was modified by incorporating the form of external loads other than gravity from cables, sensors, and actuators into the balance equation.

DOI: 10.13009/EUCASS2025-044

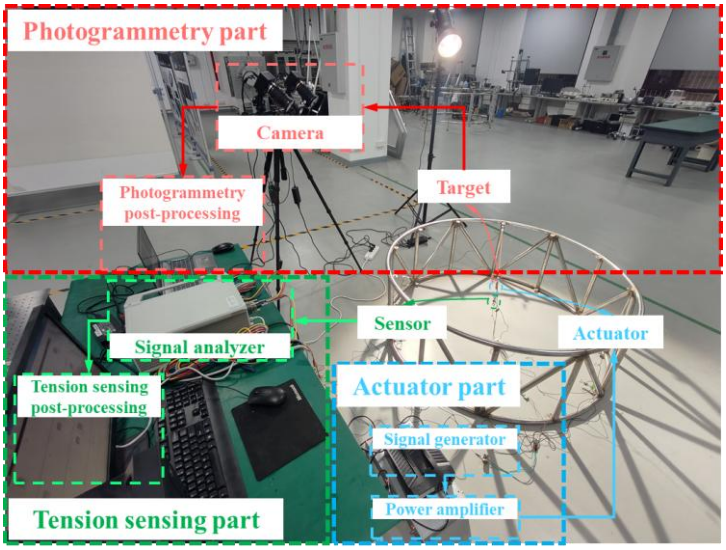
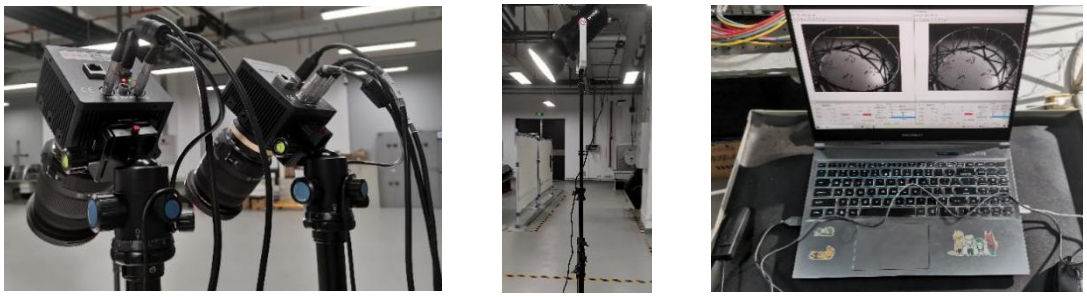


Figure 5. Experimental validation of actuator layout optimization method for mesh reflector.

The experiment mainly consists of three parts. The first part is the photogrammetric part, which is mainly used to measure the node coordinates of the reflector. Binocular photogrammetry method was used to reconstruct the three-dimensional coordinates of the target point in the experiment. Two high-resolution cameras, Revealer 5F04, JINBEI EFII-300W (LED) fill light, and post-processing equipment, were used in the experiment, as shown in the **Figure 6**. Simultaneously using a synchronous triggering device to ensure that the camera captures images of the mesh reflector simultaneously. The calibration process adopted the Zhang's calibration method.

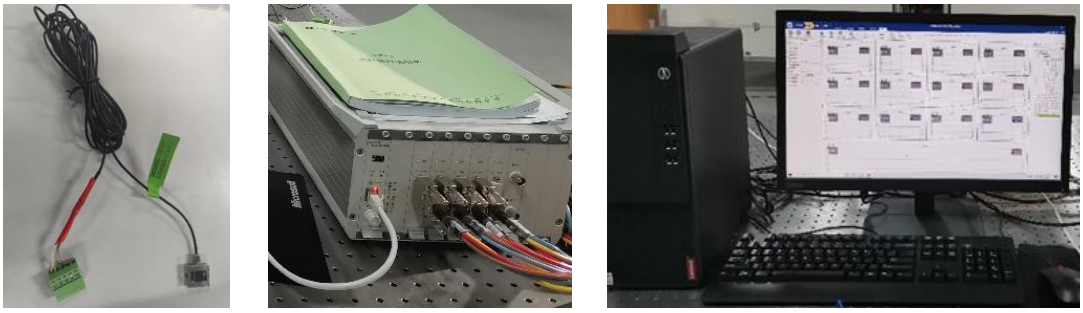


(a) Cameras (b) Fill lights (c) Post-processing equipment

Figure 6. Experimental devices used in the photogrammetric part.

The second part is the tension sensing part, mainly used for tension verification of the initial model, so that the experimental model can be as consistent as possible with the theoretical mesh reflector model. This section mainly uses SKTC-302 bridge strain sensors, DH5922D signal analyzer, and post processing equipment, which are shown in **Figure 7**. The sensor has a range of 30N and can cover the full range of cable tension changes; The resolution is 0.01N, which can effectively distinguish tension changes; The weight is 0.02kg, which can minimize the impact of sensor gravity on the structure to the greatest extent possible. Take measures to ensure that the measured values of the installed strain sensors are consistent with the cable tension. During the installation process, first connect the force sensor to the front cable net and perform a zeroing operation before the data collection instrument, which could avoid the effects of zero drift and sensor weight. Due to the presence of noise in the force sensor, to minimize the impact of noise, the data acquisition instrument simultaneously collects data with a 1-second time span, filters the data in each force sensor to eliminate the influence of random noise on the results, and takes the average of the filtered signal. The average value is used as the monitoring value of the force sensor and is substituted into the shape adjustment method for calculation. Thirteen sensors were installed in the mesh reflector test model, located as shown in the **Figure 8**. The blue lines represent the surrounding truss, the black lines represent the cables in the cable net, and the green, red, and blue rectangular boxes represent the sensors embedded in the cables.

DOI: 10.13009/EUCASS2025-044



(a) Bridge strain type force sensor (SKTC-302)

(b) Signal analyzer (DH5922D)

(c) Post-processing equipment

Figure 7. Experimental devices used in the tension sensing part.

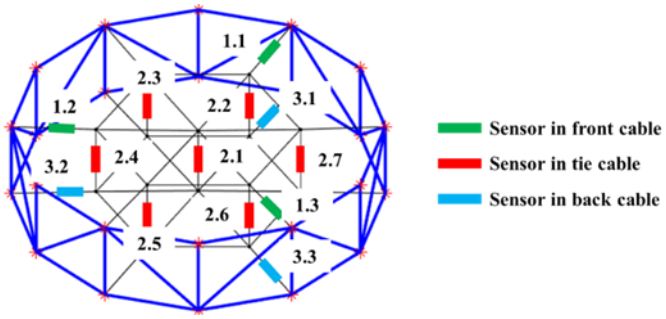


Figure 8. Locations of the sensors in the mesh reflector test model.

The third part is the actuating part, which mainly uses actuators to adjust the reflector to achieve higher reflector accuracy. This section mainly includes actuators, signal generators, and power amplifiers, as shown in the **Figure 9**. The signal generator outputs a given sawtooth wave, which is amplified by a power amplifier and input into the actuator to achieve the actuation process. Ultimately, force sensors are used to monitor whether the actuator has achieved the specified stroke.



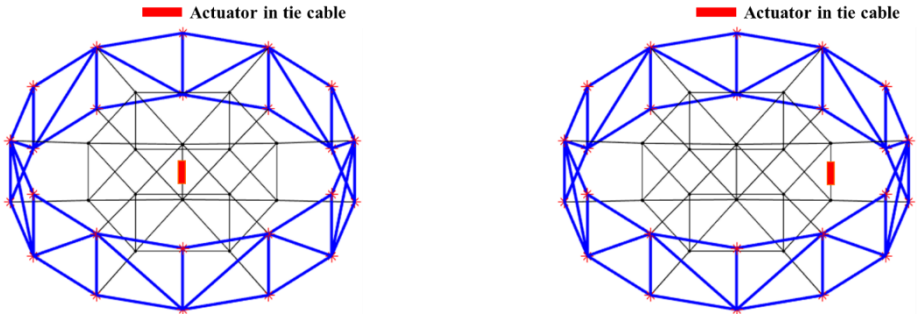
(a) Actuator

(b) Signal generator

(c) Power amplifier

Figure 9. Experimental devices used in the actuating part.

To further validate the effectiveness of the proposed method, two actuator layouts were designed, which are shown in **Figure 10**. The optimized actuator layout is ALE1, while the Unoptimized actuator layout is ALE2.



(a) Optimized actuator layout (ALE1)

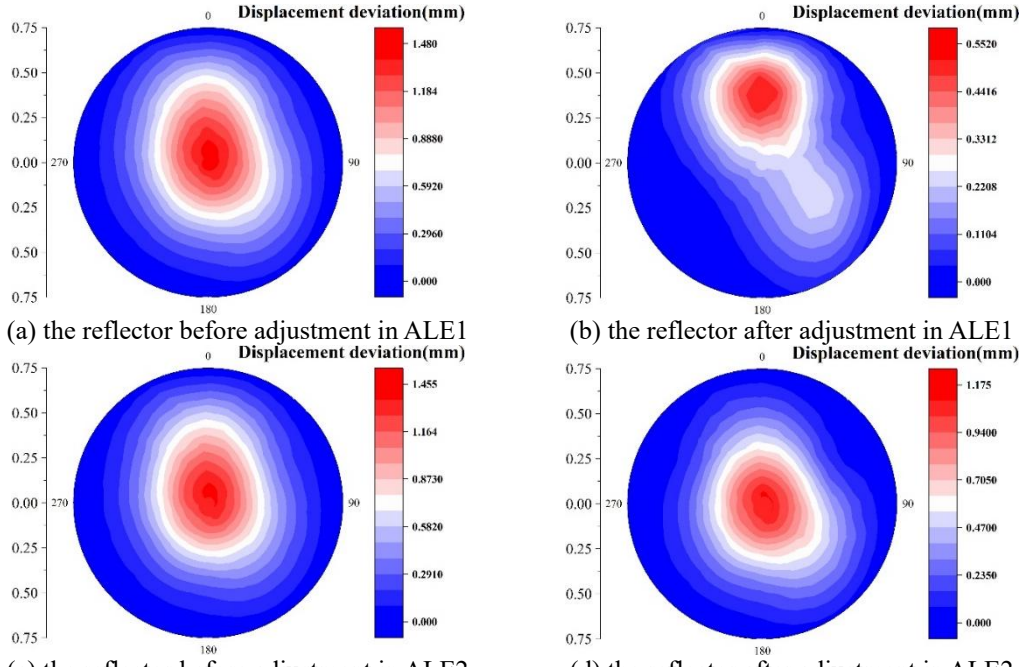
(b) Unoptimized actuator layout (ALE2)

Figure 10. The actuator layouts in the experiment.

DOI: 10.13009/EUCASS2025-044

4.2 Experiment results

Due to differences in actuator installation positions, the actuator gravity will be applied to different reflector nodes, which result in the inherent structural variations of the initial cable-net configurations of ALE1 and ALE2. However, through photogrammetry and manual adjustments implemented on the reflector, the experimental models under these two actuator layouts were rendered geometrically comparable. This study employs nodal displacement deviation contour maps to quantify positional discrepancies between nodes in actual/predicted reflectors and their counterparts in the ideal configuration. Each reflector node is uniquely identified by its x-y coordinates, with a two-dimensional polar coordinate system adopted for spatial representation. A chromatic gradient from red (indicating larger deviations) to blue (representing smaller deviations) visually encodes the magnitude of displacement errors. **Figure 11** illustrate the pre-adjustment and post-adjustment nodal deviation patterns for both actuator layouts, while **Table 3** quantitatively summarize reflector accuracy metrics and actuator adjustment efficacy before and after shape adjustments.



(a) the reflector before adjustment in ALE1 (b) the reflector after adjustment in ALE1

(c) the reflector before adjustment in ALE2 (d) the reflector after adjustment in ALE2

Figure 11. Comparison of displacement deviation of cloud charts of the reflectors before and after adjustment under ALE1 and ALE2.

Table 3. Comparison of Reflector accuracy before and after adjustment under ALE1 and ALE2.

Condition	Reflector accuracy(mm)	η
Before adjustment in Condition one	0.752	0%
Condition one	0.254	66.3%
Before adjustment in Condition two	0.708	0%
Condition two	0.515	27.3%

As illustrated in **Figure 12(a)** and **(c)**, both actuator configurations demonstrate relatively minor displacement deviations in their respective reflectors. This comparability enables direct performance evaluation between the two configurations, with tabulated data revealing a marginal surface accuracy difference of 0.044 mm. **Figure 12(b)** and **(d)** reveal persistent localized displacement anomalies following open-loop active adjustment via inertial piezoelectric actuators, a phenomenon attributed to the single-actuator configuration's limited spatial influence - primarily governing adjacent nodes while exhibiting diminished global control capability. Comparative analysis of **Figure 12(b)** and **(d)** demonstrates that the optimized actuator arrangement (ALE1) achieves superior precision in surface regulation, whereas configuration ALE2 exhibits limited effectiveness. The quantitative comparison reveals a substantial performance disparity: the ALE1 configuration attains 66.3% displacement error mitigation efficiency, contrasting sharply with ALE2's 27.3% efficacy. These empirical results systematically validate both technical feasibility and operational effectiveness of the proposed actuator layout optimization method.

DOI: 10.13009/EUCASS2025-044

5. Conclusions

This study presents a systematic approach for optimizing mesh reflector actuator layouts to achieve comprehensive performance under variable environmental disturbances. By employing a statistical analysis-based optimization framework involving 3,000 stochastic load scenarios (accounting for cable assembly errors, thermal loads, and cable stiffness degradations), the proposed method generates a universal actuator layout that balances adjustment efficiency, reflector accuracy, and operational practicality.

Simulation results demonstrate that while traditional optimization methods (e.g., the Yuan-optimized layout) achieve marginally superior surface accuracy (maximum discrepancy: 0.036 mm), their reliance on post-deployment actuator repositioning renders them impractical for operational reflectors. In contrast, the statistical analysis method attains comparable accuracy (discrepancy: 0.044 mm in experiments) without requiring layout modifications, ensuring robustness across diverse load conditions. Experimental validations further confirm the technical superiority of the optimized layout (ALE1), which achieves 66.3% displacement error mitigation efficiency—a 2.4-fold improvement over the suboptimal configuration (ALE2: 27.3%). The persistent localized displacement anomalies observed in ALE2 highlight the limitations of actuator arrangements with restricted spatial influence, underscoring the necessity of systematic optimization for global control capability.

These findings collectively validate that the proposed method not only resolves the critical challenge of balancing precision and practicality in actuator placement but also establishes a generalizable framework for designing adaptive reflector systems resilient to on-orbit uncertainties.

References

[1] Liu, S; Liu, X; Li, G; Zhang, S; Zheng, S; Wang, B; Xie, S; Xu, M, A novel identification approach of mesh reflector based on tie cable tension sensing. Acta Astronautica, 2024, 215: 277-295.

[2] Du, J; Zong, Y; Bao, H, Shape adjustment of cable mesh antennas using sequential quadratic programming. Aerospace Science and Technology, 2013, 30(1): 26-32.

[3] Zhou, M; Yang, J; Zheng, H; Song, W, Design and shape adjustment of developable surfaces. Applied Mathematical Modelling, 2013, 37(6): 3789-3801.

[4] Wang, Z; Li, T; Cao, Y, Active shape adjustment of cable net structures with PZT actuators[J] Aerospace Science and Technology, 2013, 26(1): 160-168.

[5] Yuan, S; Jing, W, Optimal shape adjustment of large high-precision cable network structures. AIAA Journal, 2021, 59(4): 1441-1456.